Iron-modified biochar-based bilayer permeable reactive barrier for Cr(VI) removal

Ziyi Zhou[a], Peng Liu[a,*], Sheng Wang[c], Y. Zou Finfrock[b], Zhihang Ye[a], Yu Feng[a]

Xiaodan Li[d]

[a] *School of Environmental Studies & State Key Laboratory of Biogeology and Environmental Geology, China University of Geosciences, Wuhan 430074, China*

[b] *Structural Biology Center, X-ray Science Division, Argonne National Laboratory, Lemont, IL 60439 USA*

[c] *Zhejiang Geological Prospecting Institute, China Chemical Geology and Mine Bureau, Hangzhou 310000, China*

[d] *China Northeast Municipal Engineering Design and Research Institute Co. Ltd., Changchun 130021, China*

*Corresponding author: E-mail: pengliu@cug.edu.cn (P. Liu).

ABSTRACT

Iron (Fe)-modified biochar (FeBC) has been developed to remove hexavalent chromium (Cr(VI)) from groundwater and is suitable for use in permeable reactive barriers (PRBs). However, Cr(VI) removal behavior and chemical processes in FeBC-based PRBs are not fully understood, and the potential for Fe release has not been addressed. In this study, three FeBC-based PRBs were assessed in column experiments for 563 days with respect to their ability to remove Cr(VI). Bilayer column filled with FeBC+limestone and BC+limestone in two separate layers (FeBC_Ca_BC) showed the best performance in terms of Cr(VI) removal with a low treatment cost. The corrosion of FeBC was mainly related to pH and Cr(VI) concentration rather than flow rate. Leached Fe was attenuated by BC and limestone and reutilized in FeBC_Ca_BC. Cr(VI) was reduced to Cr(III) and then adsorbed or precipitated on the biochars. Cr and Fe formed inner-sphere complexes and then transformed from double corner sharing to edge sharing. During the reaction, Cr penetrated from the surface to the interior of the biochars and became a more stable species. This study provides evidence of the effectiveness of a new combination of biochars for Cr(VI) removal and insights into the reaction mechanisms.

Environmental implication

Chromium (Cr) is a typical contaminant in groundwater that originates from industrial processes. Fe-modified biochar (FeBC) is an efficient material for remediating Cr(VI)-contaminated solution, but the potential for Fe release is a concern. Moreover, Cr(VI) removal behavior and chemical processes in FeBC-based

PRBs are not fully understood under long-term conditions. Our study developed an FeBC-based bilayer PRB to remediate Cr(VI)-contaminated groundwater and attenuate Fe release. A corner-sharing configuration intermediate was observed and a more detailed mechanism of Cr(VI) removal was proposed. The mechanism indicated the removed Cr has good stability that increased with time.

Keywords: Cr(VI), Fe-modified biochar, XAS, CMXRFI, Removal mechanism.

1 Introduction

Hexavalent chromium (Cr(VI)) is a common heavy metal contaminant due to its high solubility, migration, and toxicity, and is identified as one of the top toxic contaminants by the United States Environmental Protection Agency (USEPA) (An et al., 2018). Surface waters and groundwaters around the world have been contaminated with Cr(VI) due to industrial activities such as metallurgy, metal plating, chromate manufacturing, textile dyeing, and tanneries. Trivalent Cr (Cr(III)) has a lower toxicity than Cr(VI) and is prone to precipitation in the form of hydroxides, oxides, or oxyhydroxides (Zhong et al., 2017). Therefore, the reduction of Cr(VI) to Cr(III) is considered an effective method to remediate Cr(VI)-contaminated water (Kantar et al., 2015).

Permeable reactive barriers (PRBs) are an effective and economical remediation technique for contaminated groundwater (Blowes, 2002; Blowes et al., 1997; Li et al., 2022b; Lu et al., 2017; Richard and Biester, 2016; Zhang et al., 2021). PRBs, filled with reactive medium, can be installed in the flow path of Cr(VI)-contaminated groundwater; when the contaminated groundwater flows through the PRB, Cr(VI) is

59 removed by reacting with the active materials.

60 The Cr(VI) removal efficiency of a PRB largely depends on the filling material.
61 Over the past three decades, the most common reactive material used in PRBs has
62 been zero-valent iron (Fe) (ZVI) (Noubactep, 2022). However, ZVI is costly and non-
63 porous, and only the surface fraction is involved in the reaction. The immediate
64 contact of Cr(VI) with fresh ZVI leads to the formation of a passivation film on the
65 ZVI, which decreases its reactivity; *in situ* cementing agents can also form and block
66 the pore spaces, resulting in a loss of permeability (Guo et al., 2016). Moreover, Fe
67 leaching is commonly reported as a potential concern during long-term monitoring of
68 ZVI PRBs (Wilkin et al., 2005). Existing PRBs lack the ability to reutilize leached Fe,
69 resulting in the loss of Cr(VI) removal efficiency and the risk of potential secondary
70 contamination.

71 Biochar, as an environmentally friendly and low-cost carbon-rich material, is
72 widely used in contamination remediation including that focusing on Cr(VI) (Zhao et
73 al., 2021). The development of biochars with a higher removal capacity (Choudhury
74 and Lansing, 2020) and the effect of combining biochars with other remediation
75 methods (Tu et al., 2020) have been widely studied. Our previous research developed
76 an Fe-modified biochar (FeBC) that showed a high Cr(VI) removal capacity (67.4 mg
77 g^{-1}) in batch-style experiments under anaerobic conditions (Feng et al., 2020; Su et al.,
78 2021). Fe^0 and Fe oxides are the primary Fe species in FeBC, and elevated Fe
79 concentrations are observed in solution after FeBC addition (Su et al., 2021). Previous
80 research mainly focuses on neutral and acidic conditions due to the faster passivation

that occurs on the biochar surface at high pH conditions; alkaline groundwater environments also significantly affect the long-term performance of FeBC-based PRBs (Huang et al., 2021). Additionally, few studies have examined Fe leaching from FeBC during Cr(VI) removal.

In this study, biochar-based bilayer PRBs were developed to remediate Cr(VI)-contaminated groundwater. We used combinations of FeBC, pristine biochar (BC), and other filling materials (silica sand or limestone) in PRBs with the aim to remove Cr(VI) and evaluate Fe retention. The silica sand and limestone were respectively used as a support material (Sleiman et al., 2016) and pH buffering agent. The long-term column experiments were conducted for 563 d (~200 pore volumes (PV)). Aqueous geochemical analyses were performed on the column effluent and from profile port samples to investigate the temporospatial evolution of Cr(VI) removal. Solid samples were collected and characterized using X-ray diffraction (XRD), Fourier-transform infrared spectroscopy (FT-IR), X-ray photoelectron spectrometry (XPS), and synchrotron-related techniques (X-ray absorption spectroscopy (XAS) analyses to determine speciation and confocal micro-X-ray fluorescence imaging (CMXRFI) for spatial distribution). The characterization results helped to evaluate Cr removal mechanisms and the stability of Cr immobilized by the FeBC. The results of the present study indicate the optimized combination of materials in a bilayer PRB can maintain long-term reactivity as well as address issues presented in previous studies related to both Fe leaching and low pH.

2 Materials and methods

2.1 Materials

Poplar wood, which is inexpensive and readily available, was used to prepare the biochars. The biomass was crushed and sorted with a sieve. Some of the biomass (0.5-2 mm) was soaked in 0.5 mol L^{-1} $FeCl_3$ solution for 2 d and dried in an oven at 60 °C. The pretreated biomass and pristine biomass were then pyrolyzed in a tube furnace (STG-60-12, Chongqing Songlang Inc., China) at 900 °C for 2 h under O_2-free conditions, following our previous method (Su et al., 2021), to respectively create Fe-modified (FeBC) and unmodified (BC) biochars.

2.2 Column experiment

Silica sand and limestone were purchased from Hunan Province, China (0.5-2 mm). The column experiment included storage bottles, pumps (K01, Zhongshan Gaoshuo Electronics Co., Ltd., China), columns, sampling cells, and output reservoirs (Fig. 1). Each column was 30.4 cm long with an internal diameter of 6 cm. Both ends were filled with 0.7 cm of silica sand to separate the reactive mixture from the influent and effluent ports and facilitate uniform water distribution. The remaining parts of the columns (29 cm) were filled with reactive materials to remove Cr(VI) from the solution.

Three columns with different mixtures of reactive materials totaling a length of 29 cm were set up. The first column (FeBC_Si) was packed with FeBC/silica sand at a volume ratio (R_v) of 1:1 to evaluate Cr(VI) removal and the release of Fe. The second column (FeBC_Si_BC) was filled with FeBC/silica sand in the first layer (lower half) (R_v: 1:1) and BC/silica sand in the second layer (upper half) (R_v: 1:1) to

investigate the feasibility of Fe attenuation by BC. BC is theoretically effective at immobilizing leached Fe due to its high cation exchange capacity (Trakal et al., 2014), and can also directly adsorb Cr(VI) (Su et al., 2021). Its inclusion in the second column directly addresses the needs identified in our preliminary study with respect to limiting Fe leaching from FeBC during Cr(VI) removal and enhancing Cr(VI) removal. The third column (FeBC_Ca_BC) was filled with FeBC/limestone in the first layer (R_v: 1:1) and BC/limestone in the second layer (R_v: 1:1) to further attenuate released Fe. The limestone was added to this column to assess its ability to neutralize the acidity of the biochars without influencing the chemical properties of the groundwater.

A Cr(VI) input solution (10 and 50 mg/L; increased after ~12 weeks; Table 1) was prepared by dissolving $K_2Cr_2O_7$ in $CaCO_3$-saturated solution to simulate Cr(VI) contaminated groundwater. The input solution was saturated in $CaCO_3$ because groundwater is usually in dissolution equilibrium with calcite (Wiegand, 2009). All analytical grade reagents were purchased from Sinopharm Chemical Reagent Co., Inc., China. Profile sampling was conducted along the column at 3.8 and 6.5 cm intervals for the aqueous and solid phases, respectively (Fig. 1). The liquid and solid sampling ports were numbered L1 to L8 and S1 to S5 from bottom to top, respectively.

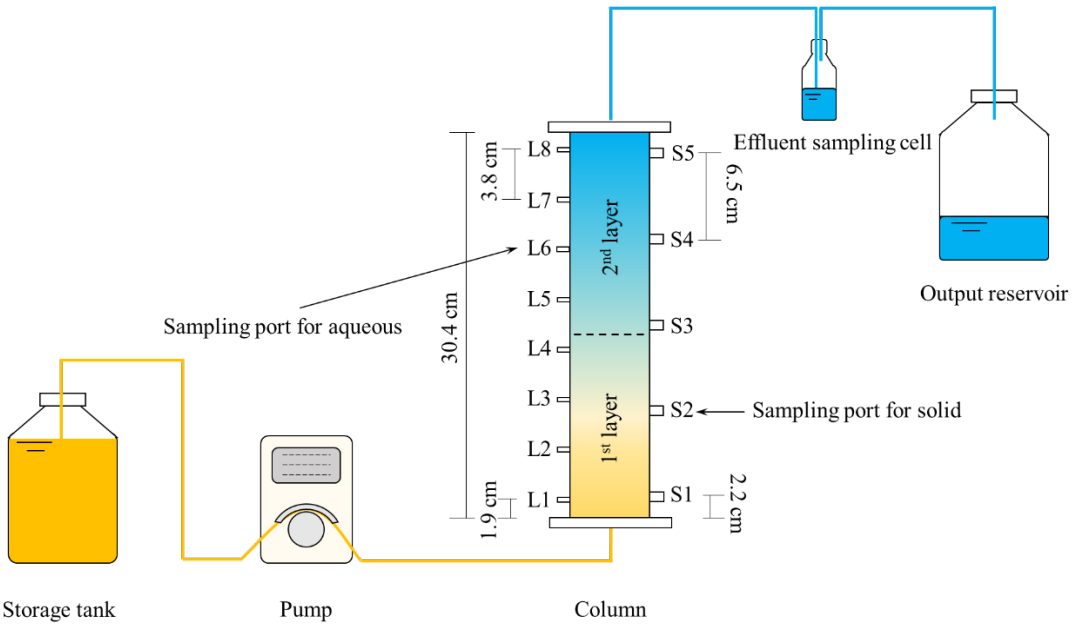

Figure 1. The column experimental setup. Yellow and blue represent Cr(VI)-contaminated influent and Cr(VI)-free effluent, respectively. Cr(VI)-contaminated solution was pumped from the storage tank upward through the column; effluent was collected in a sampling cell; and excess sample flowed into the output reservoir for further treatment before disposal. Each column included eight ports (L1-L8) for aqueous and five ports (S1-S5) for solid profile sampling.

Table 1. Flow rate and Cr(VI) concentration in each column for different stages.

	Stage	PV	Weeks	Q (PV d^{-1})	Cr(VI) (mg L^{-1})
FeBC_Si	I	0-14.0	0-6.3	0.32	10
	II	14.0-39.3	6.3-12.0	0.63	10
	III	39.3-55.2	12.0-15.6	0.63	50
	IV	55.2-	15.6-	0.32	50
FeBC_Si_BC	I	0-14.1	0-6.5	0.31	10
	II	14.1-40.1	6.5-12.4	0.63	10
	III	40.1-57.2	12.4-16.3	0.63	50
	IV	57.2-	16.3-	0.31	50
FeBC_Ca_BC	I	0-13.9	0-6.4	0.31	10
	II	13.9-40.9	6.4-12.6	0.62	10
	III	40.9-54.0	12.6-15.6	0.62	50
	IV	54.0-	15.6-	0.31	50

The columns were first flushed with CO_2 gas for 2-3 h to replace atmospheric air; the CO_2 also facilitates saturation of the columns. $CaCO_3$-saturated solution was then used to saturate the columns from the bottom. The PV was calculated based on the mass increase in the column after saturation. The Cr(VI) input solutions passed through each column at a flow rate of 10 or 20 cm d^{-1} and a concentration of 10 or 50

mg L^{-1}; the inflows of Cr(VI) input solution were divided into four stages to investigate the effects of flow rate and Cr(VI) concentrations on Fe leaching (Table 1). Effluent samples were collected from the sampling cell every 2-4 d and profile samples (L1-L8) were collected every 3-4 weeks. Solid samples, including unreacted FeBC, FeBC from FeBC_Si (S1, S3, and S5 ports), and FeBC, BC, and limestone from FeBC_Ca_BC (S1, S3, and S5 ports), were collected at PV=0, PV=102 (36.5 weeks), and PV=92 (33.1 weeks), respectively.

2.3 Aqueous analysis

Aqueous samples were immediately subjected to pH and Eh measurements under anaerobic conditions in a laboratory-designed cell using PHC101 and MTC101 electrodes (HACH, USA), respectively. The remaining samples were filtered (nylon; 0.22 μm) before alkalinity and Cr(VI) analyses. One aliquot was preserved with concentrated HCl for total Fe (tFe) and Fe^{2+} analyses. Alkalinity was immediately measured using a Hach digital titrator. Cr(VI) analysis was performed using the 1,5-diphenylcarbazide spectrophotometric method. The cumulative removed Cr(VI) mass (CRM) and the average Cr(VI) removal content of FeBC (AAC_{FeBC}) were calculated using Eqs. 1 and 2, respectively:

$$CRM_n = C_{i,n}Q_n\Delta t - \frac{(C_{e,n}+C_{e,n-1})}{2}Q_n\Delta t + CRM_{n-1}, \quad (1)$$

$$AAC_{FeBC} = CRM_{last}/m_{FeBC}, \quad (2)$$

where CRM_n (mg), CRM_{n-1} (mg), and CRM_{last} (mg) are the current, previous, and last cumulative removed Cr(VI) mass, respectively; $C_{i,n}$ (mg L^{-1}) and $C_{e,n}$ (mg L^{-1}) are the concentrations of Cr(VI) in the influent and effluent for the *nth* sampling, respectively;

Q_n is the flow rate (L min^{-1}); m_{FeBC} (g) is the mass of FeBC in the column; and Δt (min) represents the interval time between the *nth* and *(n-1)th* sampling events.

The concentrations of Fe^{2+} were immediately determined after filtration using the 1,10-phenanthroline spectrophotometric method. The concentrations of tFe were analyzed by reducing Fe^{3+} to Fe^{2+} using hydroxylammonium chloride before applying the spectrophotometric method. The results indicate all Fe present was in the form of Fe^{2+}; therefore, only tFe data are presented and discussed.

2.4 Solid phase characterization

The solid samples from FeBC_Si and FeBC_Ca_BC were immediately freeze-dried and preserved under anaerobic conditions. The mineral composition and crystallinity of the biochars were analyzed by a D8 Advance XRD (Bruker, Germany) with a radiation current of 40 mA and radiation voltage of 40 kV. The surface functional groups of biochars were analyzed using FT-IR (Nicolet IS10, USA) in a scanning range from 400-4000 cm^{-1}. The surface chemical composition and chemical states of biochars were analyzed using an EscaLab 250Xi XPS (Thermo Fisher Scientific, USA); the energy was calibrated using the C1s binding energy of 284.7 eV.

CMXRFI analyses of biochars and limestone were performed at the Advanced Photon Source (APS, USA) Beamline 20-ID. The incident beam was focused at ~2 × 2 μm^2. Samples were fixed on quartz slides using epoxy (Devcon 5 Minute Fast Drying Epoxy, USA). The full XRF spectra were collected by a high precision stage (Aerotech, Inc.). Data were corrected in MATLAB® following a method developed by Liu et al. (2017).

198 Cr K-edge XAS spectra of biochars were measured at APS Beamlines 9- and 20-
199 BM in fluorescence mode. The spectra of Cr foil, Cr_2O_3, $Cr(OH)_3$, and $K_2Cr_2O_7$ were
200 also analyzed in transmission mode as references. Each sample was scanned three to
201 five times, and the spectra merged for further data processing. XANES spectra were
202 analyzed by linear combination fitting (LCF) using ATHENA (Ravel and Newville,
203 2005). Further details of sample preparation, data collection setup and method, and
204 LCF analysis are provided by Ye et al. (2022).
205 The EXAFS spectra of biochars were compared to those of reference compounds
206 in k and R space. The atomic structures of amorphous $Cr_nFe_{(1-n)}(OOH)$ and CrO(OH)
207 are similar to FeO(OH) due to their similar ionic radii (0.615 Å for Cr(III) and 0.645
208 Å for Fe(III) (Papassiopi et al., 2014)). Therefore, the crystallographic information of
209 CrO(OH) used in this study was obtained by replacing Fe in the structure of FeO(OH)
210 with Cr. The sample EXAFS spectra were modeled in Artemis using the reference
211 compounds (Ravel and Newville, 2005). The amplitude reduction factor (S_0^2, 0.8) was
212 obtained by modeling $Cr(OH)_3$ spectra (Su et al., 2021), with other parameters kept as
213 variables. The following criteria were considered when evaluating a reasonable fit
214 from the candidate structural models: 1) R-factor <0.01 reflecting a good fit and <0.05
215 reflecting a reasonable fit (Peña et al., 2010); 2) the absolute value of energy
216 difference (ΔE_0) between the selected E_0 and modeled E_0 is <10 eV; 3) a bond length
217 difference between the theoretical structure and modeled length <0.05 Å; 4)
218 uncertainties in fitted parameters and physical possibility of fitted parameters, e.g., a
219 fit with negative values of coordination number (CN) and static disorder value (σ^2)

would be rejected; 5) visual inspection of the reproducibility between fit and data spectra in fitted k and R space (including the imaginary part) and agreement outside of the fitted range; 6) stability of fit: a good fit for a candidate model should give the same or similar fitted parameters when k-range, k-weight, R-range, and background subtraction are changed slightly; and 7) structural reasonableness of fitted parameters and models based on the known information from XANES and XRD analyses.

The Morlet wavelet transform (WT) method resolves the information in both k and R space and was used to further identify the backscattering atoms in higher coordination shells. WT was performed using the Igor Pro wavelet transform script developed by Funke et al. (2005).

3 Results and discussion

3.1 C/C_0, CRM, pH, Eh, and tFe evolution in effluent

The effluent Cr(VI) concentrations were below the detection limit (0.01 mg L^{-1}) in the first three stages and the beginning of stage IV for all of the columns (Fig. 2a). Cr(VI) was first observed at 116, 84, and 81 PVs (42.7, 28.7, and 28 weeks) in the effluent from FeBC_Si, FeBC_Si_BC, and FeBC_Ca_BC, respectively. The concentration of Cr(VI) in the effluent (C) was similar to the influent (C_0), i.e., (C/C_0) reached 1 in FeBC_Si_BC at 137 PVs (53.1 weeks); however, in FeBC_Si and FeBC_Ca_BC this ratio only reached and stabilized at 0.94 and 0.9, respectively, by the end of the experiment, indicating some Cr(VI) was still being retained by the columns. The CRM peaked at 2680, 1490, and 1540 mg for FeBC_Si, FeBC_Si_BC, and FeBC_Ca_BC, respectively, at the end of the experiment (Fig. 2b).

FeBC_Si achieved a high removal efficiency and had Cr(VI)-free effluent for the longest (~34% longer than other two columns); this is attributed to the greater amount of FeBC (70.1 g) in the FeBC_Si column than in either the FeBC_Si_BC or FeBC_Ca_BC columns (both 32.1 g). However, FeBC_Ca_BC contained the lowest final Cr(VI) C/C_0, which demonstrates an enhanced potential for Cr(VI) remediation through the use of BC and limestone. Notably, the experiment was interrupted for 1.2-5.7 PVs (0.6-2.5 weeks) by the COVID-19 pandemic (evident in C/C_0 data in Fig. 2(a)). During the interruption, the valves of the influent and effluent ports were closed to stop the experiment. The residual solution was still in contact with the reactive materials, resulting in the low Cr(VI) C/C_0 (<0.05) at the restart of the experiments.

To quantitatively estimate the contribution of FeBC in the system, Cr(VI) adsorption by the limestone (0.0155 mg g^{-1}; Aziz et al. (2008)) and the BC (1.03 mg g^{-1}; He et al. (2019)) were considered and excluded, with all remaining Cr(VI) removal assumed to be due to FeBC. The AAC_{FeBC} was 38.1 mg g^{-1} for FeBC_Si, which is lower than both FeBC_Si_BC (45.4 mg g^{-1}) and FeBC_Ca_BC (46.1 mg g^{-1}). The higher AAC_{FeBC} in FeBC_Ca_BC indicates Cr(VI) removal is enhanced by the addition of BC and limestone. The AAC_{FeBC} of FeBC_Ca_BC in this study is ~40 times greater than the AAC_{ZVI} of ZVI (CC-1004 Connelly-GPM, Inc., USA) (Tables S1&S2)-filled columns (~1.13 mg g^{-1}; Jamieson-Hanes et al. (2015)). Although the price of FeBC ($1.02 USD kg^{-1}; Li et al. (2022a)) is similar to CC-1004 ZVI ($1.02 USD kg^{-1}), the estimated Cr(VI) treatment cost per kilogram of Cr(VI) for the FeBC_Ca_BC PRB ($22.10 USD kg^{-1}) is only ~2.51% that of the CC-1004 ZVI PRB

($881 USD kg^{-1}). The actual costs may differ from these estimates because the performance of every ZVI PRB is different and depends on many factors such as the composition of the ZVI, particle size, and more.

Determining the half-life is key to evaluating PRB designs, as it affects the performance and cost. The half-life of FeBC_Si in this experiment was 151 PVs, higher than a ZVI column mixed with Cr(VI)-reducing bacteria (~150 PVs) (Zhong et al., 2017). FeBC_Si_BC and FeBC_Ca_BC were filled with only half the mass of FeBC as FeBC_Si, and reached half-lives of 88 and 94 PV, respectively. Furthermore, if the removal of Cr(VI) by BC and limestone is ignored, the half-lives per gram of FeBC from FeBC_Si, FeBC_Si_BC, and FeBC_Ca_BC were 2.15, 2.74, and 2.98 PVs, respectively. The FeBC in FeBC_Ca_BC showed the longest half-life and the greatest potential for Cr(VI) removal.

The AAC_{FeBC} of all of the columns in this study were between values of 30.2 mg g^{-1} (aerobic) and 67.4 mg g^{-1} (anaerobic) determined in the related batch study (Su et al., 2021). In the present experiment, the columns were initially anaerobic, but the storage tank and output reservoir were open to the atmosphere to simulate groundwater field conditions. O_2 replenished from the atmosphere was likely the reason for the intermediate value of AAC_{FeBC} determined here.

The initial effluent pH in all of the columns was lower than the influent pH, reflecting the acidity of FeBC (Fig. 2c); this is consistent with values from the recent batch experiment (Su et al., 2021). Increases in the effluent pH of all of the columns from the initial value of ~6.9 to 7.2-8.5 were observed with the removal of Cr(VI) in

stages II and III, indicating the consumption of H^+. The effluent pH of FeBC_Si_BC and FeBC_Ca_BC increased sharply from ~8 to ~10 at 81 and 84 PVs, respectively, while the effluent pH of FeBC_Si (8.5-8.9) was more stable. The rapid increase in the effluent pH was only observed in the columns that contained BC, and coincided well with the time when Cr(VI) was observed in the effluent. Notably, these trends (rapid increase and consistency) were observed in the effluent samples but not the profile samples. This consistency is likely due to the involvement of O_2 in the reaction near the outlet end and the consumption of H^+ by Fe^{2+} during Cr(VI) removal (Su et al., 2021). The leached Fe^{2+} accumulated on BC, further increasing the consumption of H^+ and causing the rapid increase of pH in the effluent of FeBC_Si_BC and FeBC_Ca_BC. The effluent pH dropped to relatively steady values in all three columns (~7.8 for FeBC_Ca_BC and ~7.6 for the others) by the end of the experiment.

The initial effluent Eh of all of the columns was lower than the influent, reflecting a reducing environment (Fig. 2d). The effluent Eh of the columns increased over time and nearly stabilized at the influent Eh (~502 mV) when the effluent Cr(VI) reached the highest concentration measured. The overall effluent Eh values of FeBC_Si_BC and FeBC_Ca_BC were similar, whereas the effluent Eh of FeBC_Si was lower due to the higher FeBC dosage, reflecting stronger reducibility.

The tFe concentration is a major parameter of concern as secondary contamination of Cr-contaminated waters with Fe is undesirable. FeBC contained Fe(0), and Fe^{2+} could leach from the surface of Fe(0) (Diao et al., 2016). FeBC-based PRB is a more efficient PRB to remove Cr(VI) with higher activity and longer

running time than ZVI PRB (~80 days, Huang et al. (2021)). Therefore, Fe in FeBC-based PRB is easier to be released into the solution than ZVI PRB (~100 mg L^{-1}, Huang et al. (2021)). Moreover, the Fe leached from FeBC was also observed in the previous batch study (80 mg L^{-1}, Su et al. (2021)). The higher concentration of leached Fe in this column experiment than FeBC in the batch experiments is attributed to the higher solid-liquid ratio at the beginning of the column experiment. The tFe concentration then sharply decreased to 12.0, 18.9, and 0.4 mg L^{-1} after 5 PVs and was continually detected for 59.9, 23.5, and 5.4 PVs in effluent from FeBC_Si, FeBC_Si_BC, and FeBC_Ca_BC, respectively. FeBC_Ca_BC achieved the greatest Fe immobilization and Cr(VI) removal efficiency, demonstrating the benefit of immobilizing the released Fe on BC and limestone with concurrent Cr(VI) removal.

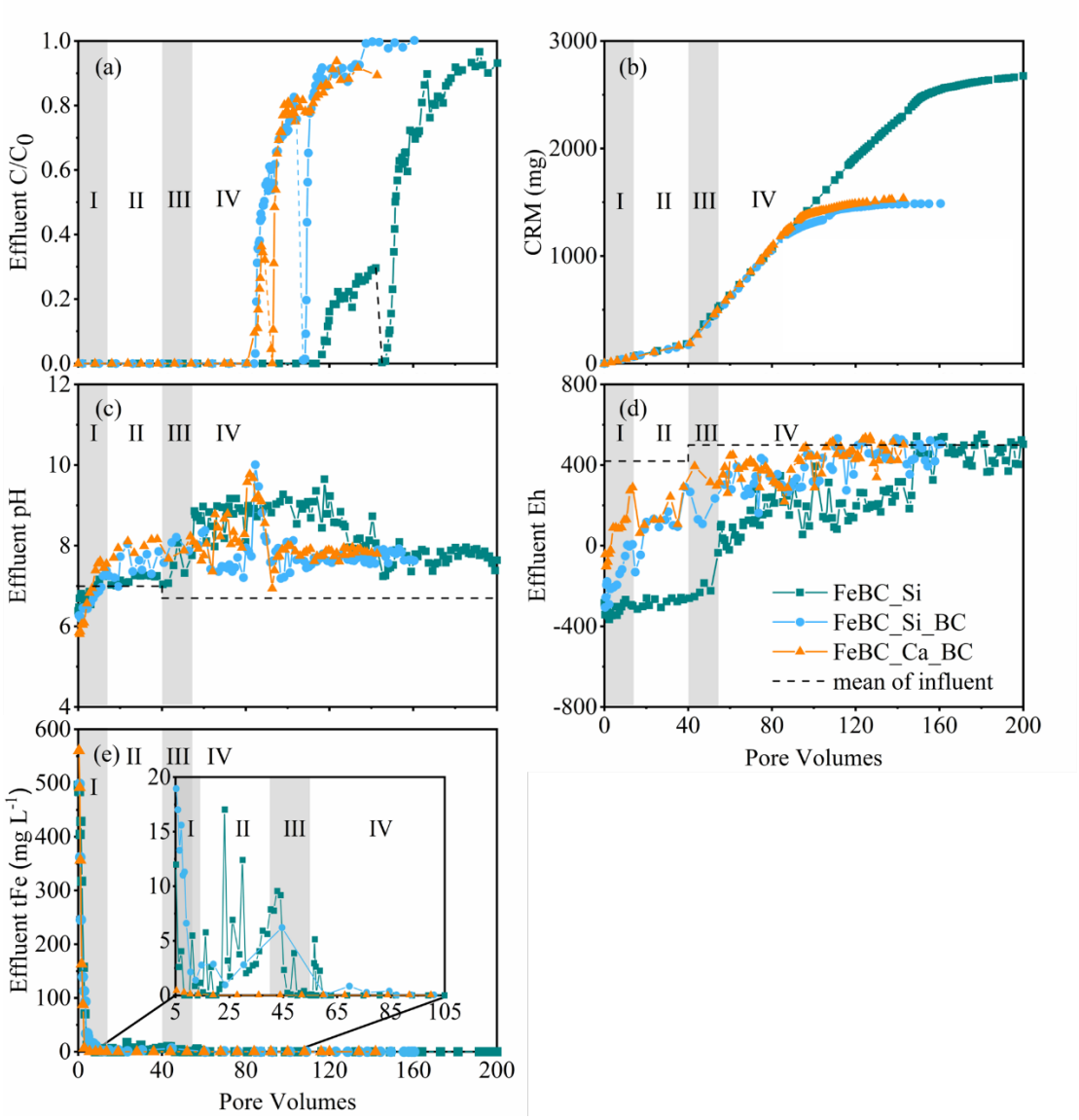

Figure 2. (a) Effluent Cr(VI) C/C_0 (breakthrough) curves, (b) CRM, (c) pH, (d) Eh, and (e) tFe concentrations from the three experimental columns; the subplot in (e) represents the details of effluent tFe concentrations between 5 and 105 PVs. Shaded blocks represent the four experimental stages. The dashed colored lines in (a) reflect the interruption due to COVID-19. The dashed black lines in (c) and (d) reflect the mean of the influent pH and Eh, respectively.

3.2 Profile C/C_0 and tFe

The Cr(VI) profile front of all of the columns demonstrated similar trends in the first three stages (Fig. 3(a-c)). The C/C_0 gradually increased to 0.72 at the lowest port (1.9 cm) in stage I and remained stable in stage II. In stage III, the Cr(VI) front migrated to 24.1 cm in FeBC_Si and 13.3 cm in the other columns due to the

increased influent Cr(VI) concentration (i.e., increased from 10 to 50 mg/L after ~12 weeks). In stage IV, the migration trend of the Cr(VI) front within FeBC_Si remained steady until the end of the experiment. Meanwhile, the Cr(VI) fronts in FeBC_Si_BC and FeBC_Ca_BC moved forward as noted for FeBC_Si at the beginning; however, the movement of the Cr(VI) fronts in these columns was delayed near the layer boundary (~14 cm). After breaking through the boundary, the Cr(VI) front rapidly migrated and reached the end of both columns in ~9.7 PVs.

Aqueous analysis showed the different degrees of Fe release from FeBC in the column profile after 10 PVs (Figs. 3d-f). In FeBC_Si, high concentrations of tFe were distributed across the column except for the inlet in stage I and II. The results of the first two stages reveal that the leaching of Fe was not sensitive to the flow rate. In stage III, the concentration of tFe in FeBC_Si decreased to <10 mg L^{-1} concurrent with the increase in Cr(VI) concentration. Moreover, the front of the low tFe area (<10 mg L^{-1}) was highly consistent with the Cr(VI) front, providing evidence of the Fe consumption in Cr(VI) removal. The maximum tFe concentration was lower in FeBC_Ca_BC (<2 mg L^{-1}, Fig. 3f) compared to that in FeBC_Si_BC (<10 mg L^{-1}, Fig. 3e) and FeBC_Si (<20 mg L^{-1}, Fig. 3d), indicating both BC (Eq. 3) and limestone (Eqs. 4&5) contribute to Fe immobilization. Furthermore, a decrease in tFe concentrations and increase in pH (Fig. S1) were observed in the first layers (FeBC/sand) of FeBC_Si_BC and FeBC_Ca_BC. This correlation suggests the limestone and BC in the second layers of these columns not only immobilize the leached Fe but also attenuate the corrosion of FeBC by neutralizing the acidity in the

first layers.

$$\equiv R + Fe^{2+} \rightarrow \equiv R - Fe, \quad (3)$$

$$CaCO_3 \rightarrow Ca^{2+} + {CO_3}^{2-}, \quad (4)$$

$$2Fe^{2+} + 2OH^+ + {CO_3}^{2-} \rightarrow Fe_2(OH)_2CO_3, \quad (5)$$

where ≡R represents the biochar surface matrix.

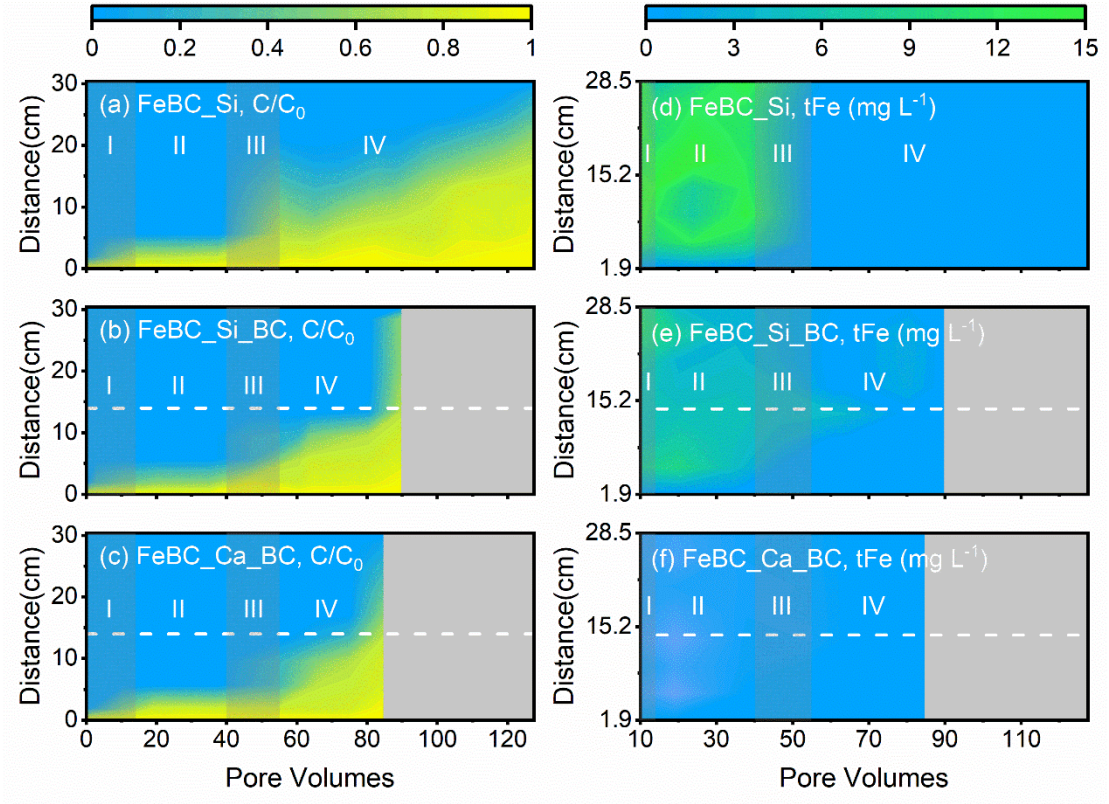

Figure 3. The profile C/C_0 of Cr(VI) in (a) FeBC_Si, (b) FeBC_Si_BC, and (c) FeBC_Ca_BC; tFe concentrations after 10 PVs in (d) FeBC_Si, (e) FeBC_Si_BC, and (f) FeBC_Ca_BC. The white dashed line is the boundary between the reactive material (FeBC) and the BC/sand or BC/limestone mixture.

3.3 Solid phase analysis

3.3.1 XRD

The XRD results show the unreacted FeBC contained Fe^0, maghemite, and akageneite (Fig. 4a). The diffraction peak intensities in FeBC from FeBC_Si and FeBC_Ca_BC increased after reaction and reached the highest value at S1 in FeBC_Si, revealing FeBC was corroded by the Cr(VI) solution. However, spectra for

the S1 sample from FeBC_Ca_BC do not show a similar high intensity, indicating BC and limestone can mitigate the excessive corrosion of FeBC. The diffraction peaks of maghemite and akageneite present in the unreacted sample disappear in the S1 sample from FeBC_Si in the high Cr(VI) concentration zone (~46 mg L^{-1}, at 102 PVs). On the contrary, the diffraction peaks of maghemite remain in low Cr(VI) concentration zones (~26 mg L^{-1} for S3 in FeBC_Si and ~2 mg L^{-1} for S5 in FeBC_Si at 102 PVs, respectively) and new diffraction peaks of goethite are detected in S5 for FeBC_Si. Overall, the varieties of minerals decreased and increased under high and low concentrations of Cr(VI), respectively. Diffraction peaks of lepidocrocite are evident for BC from S3 of FeBC_Ca_BC, indicating the immobilization of Fe by BC. Lepidocrocite is more effective than goethite with respect to Cr(VI) removal and likely contributes to the high Cr(VI) removal capacity in FeBC_Ca_BC (Mineno and Okazaki, 2004). Calcite was the dominant Ca species newly generated in all of the samples due to the $CaCO_3$-saturated input solution and the limestone (for FeBC_Ca_BC).

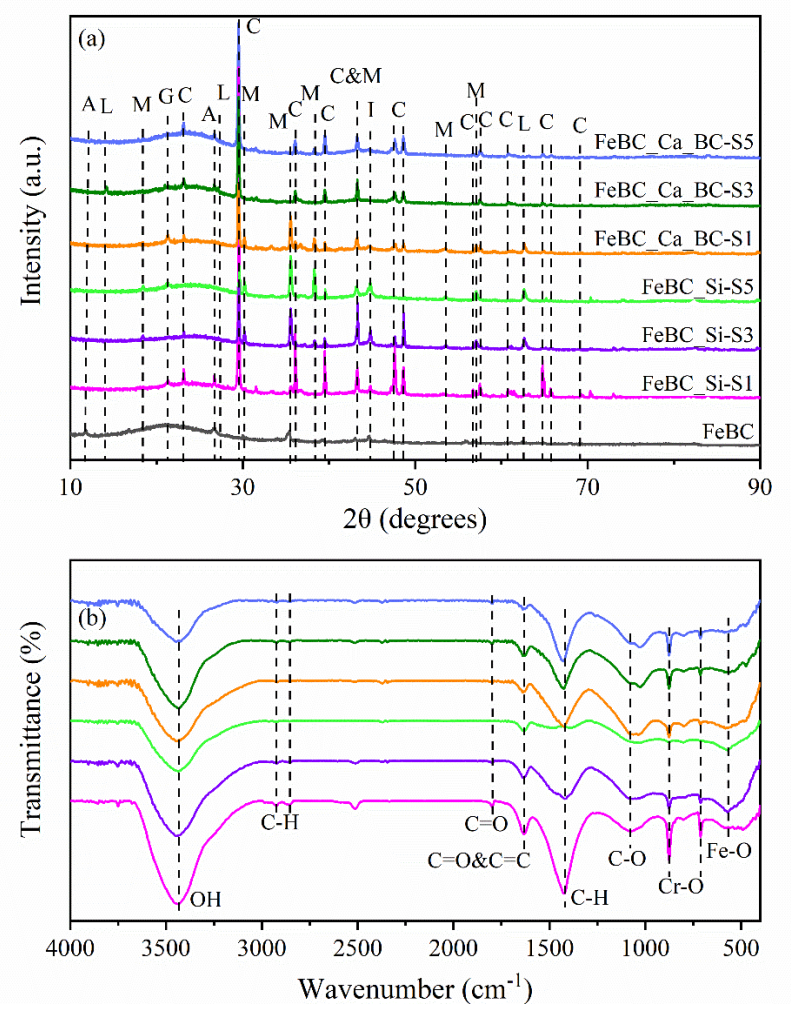

Figure 4. (a) XRD patterns of unreacted FeBC, of FeBC (ports S1, S3, and S5) from FeBC_Si collected at 102 PVs, and of FeBC (port S1) and BC (ports S3 and S5) from FeBC_Ca_BC collected at 92 PVs. Diffraction peaks are indicative of reference minerals: A, Akageneite(β-FeOOH); C, Calcite($CaCO_3$); G, Goethite(α-FeOOH); I, iron(Fe^0); L, Lepidocrocite(γ-FeOOH); M, Maghemite(γ-Fe_2O_3). (b) FT-IR spectra of FeBC and BC sampled from FeBC_Si and FeBC_Ca_BC; the legend is the same as for (a).

3.3.2 FT-IR and XPS

FT-IR spectra of the biochars indicate similar functional groups present on the surface, including -OH, C-H, C=O, C=O&C=C, C-O, and Fe-O (Fig. 4b). The stretching vibration of Cr-O is detected for all samples except FeBC from S5 for FeBC_Si, corresponding to the detection of Cr(VI) in all aqueous samples at 102 PV except in the second layer of FeBC_Si. The Fe-O group on BC from S3 and S5 for

FeBC_Ca_BC indicates Fe immobilization by BC. XPS analysis of C1s and O1s spectra identified -COO (288.5 eV), C-O (285.7 eV), C=C (284.8 eV) (Choudhary et al., 2017), C-O (533.5 eV), OH (531.7 eV), and O^{2-} (530 eV) (Chaparro et al., 2000) functional groups on all of the samples (Fig. S2). C-O is the main functional group involved in the reaction (Eq. 6; Table S3); its reducibility was also observed by Ahmed et al. (2017). XPS analysis of Fe2p and Cr2p indicated Fe and Cr are in trivalent form in the biochars (except from S1 for FeBC_Si), revealing Cr is reduced to Cr(III) and immobilized on the biochars with Fe(III). Previous studies on biochars and Fe materials also report that both Cr and Fe predominantly exist in trivalent form (Li et al., 2019; Park et al., 2008). Here, 14.3% of the total Cr(VI) removed was adsorbed on FeBC at S1 for FeBC_Si, indicating direct Cr(VI) adsorption by FeBC (Table S4).

$$\equiv R - C - O + Cr_2O_7{}^{2-} \rightarrow \equiv R - C = C + R - COO^- + Cr^{3+}. \quad (6)$$

3.3.3 Confocal micro-X-ray fluorescence imaging

The CMXRFI analysis shows the distribution of elements in biochar particles based on the absorbances (I_f/I_0) of each element (Fig. 5). Ca is an essential element for plants with relatively even distribution, and can be used to reflect the porous structure of biochars (Feng et al., 2020; Liu et al., 2020). Ca accumulated on the surface of FeBC close to the inlet (S1), with a maximum absorbance of 0.04 for FeBC_Si (Fig. 5e) and 0.6 for FeBC_Ca_BC (Fig. 5c). The accumulation of Ca on the surface of the biochars is due to calcite precipitation from the $CaCO_3$-saturated input solution or the addition of limestone (for FeBC_Ca_BC).

A fraction of the Fe loaded on the FeBC was washed away by the input solution, especially in the second layer of the columns (Fig. 5d); the maximum absorbances of FeBC_Si and FeBC_Ca_BC were the same at 3.7 in the first layer (S1). Further, the movement of Fe resulted in high Fe depletion at the beginning of the experiment, corresponding to the profile analysis (Figs. 3d-f). Fe maximum absorbances in BC (S3 and S5 for FeBC_Ca_BC) were 0.01 (Figs. 5a and 5b), distinct from the background signal and verifying the immobilization of Fe in BC, consistent with the XRD results (Fig. 4a).

CMXRFI analysis shows a Cr distribution similar to the Fe distribution. Cr was distributed not only on the surface but also in the interior of the FeBC, and penetrated deeper into FeBC as the experiment proceeded (i.e., by 36.5 or 33.1 weeks for FeBC_Si and FeBC_Ca_BC, respectively). Cr deposited deeper in FeBC particles is more stable than Cr on the surface (Liu et al., 2019a). Therefore, the Cr(VI) immobilized deeper in the FeBC particles in this study than in the batch study (Su et al., 2021) is presumed to be more stable, with a greater ability to resist environmental variations. The co-localization of Cr and Fe on the surface of the limestone indicates the limestone provides sites for the co-precipitation of Cr and Fe (Figs. 5f-h).

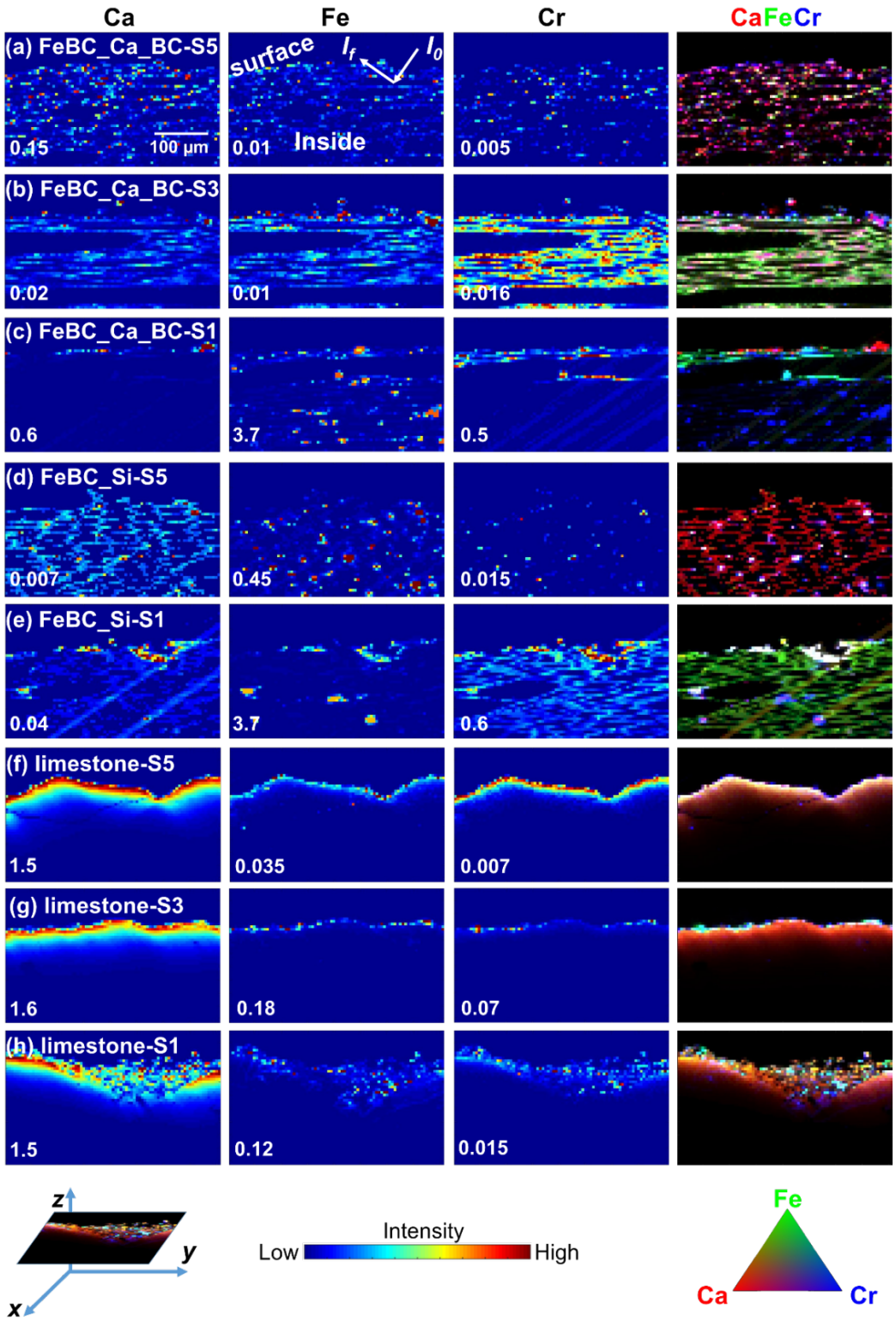

Figure 5. Elemental maps of FeBC (ports (a) S5, (b) S3, and (c) S1) of FeBC_Si collected at 102 PVs, of BC (ports (d) S5 and (e) S3) and FeBC ((f) port S1) of FeBC_Ca_BC collected at 92 PVs, and of limestone (ports (f) S5, (g) S3, and (h) S1) of FeBC_Ca_BC at PV=92 using CMXRFI. Ca, Fe, Cr, and combined tri-color maps are shown from left to right. The maximum normalized absorbances of the corresponding elements are listed in the bottom-left corner.

441 **3.3.4 X-ray absorption spectroscopy**

442 The spectra of $K_2Cr_2O_7$ and $Cr(OH)_3$ are required to fingerprint Cr(VI) and Cr(III)
443 to fit the XANES spectra of biochars. The LCF fitting results indicate the majority of
444 Cr in FeBC and BC is trivalent, except at S1 for FeBC_Si (Fig. 6a; Table 2). At this
445 location, the LCF results suggest a minor amount (5.5%) of Cr is present in
446 hexavalent form; the corresponding value from the XPS analysis is <14.3%. The
447 results for Cr(VI) content for the bulk (XAS results) and surface phase (XPS results)
448 differ due to the surface sensitivity (<10 nm in depth) of XPS (Liu et al., 2019b).
449 Therefore, these results indicate the distribution of Cr(VI) is uneven in FeBC_Si-S1,
450 with Cr(VI) mainly accumulating on the surface (Eqs. 7-10). The existence of both
451 Cr(VI) and Cr(III) on FeBC indicates both adsorption and reduction contribute to
452 Cr(VI) removal. Cr in FeBC and BC from FeBC_Ca_BC is all trivalent before 92 PVs,
453 indicating reduction makes the full contribution to Cr(VI) removal. Moreover, Cr
454 saturated in FeBC at S1 for FeBC_Si, revealing individual contributions of adsorption
455 and reduction of 5.5% and 94.5%, respectively, at the end of the experiment.

$$\equiv R + H^+ \rightarrow \equiv R(+), \quad (7)$$

$$\equiv R(+) + {Cr_2O_7}^{2-} \rightarrow \equiv R - Cr_2O_7(surface), \quad (8)$$

$$\equiv R(+) + Cr^{3+} \rightarrow \equiv R - Cr^{3+}(surface), \quad (9)$$

$$\equiv R - Cr^{3+}(suface) + Interior \equiv R \rightarrow Interior \equiv R - Cr^{3+} + \equiv R(+). \quad (10)$$

456 Unreduced Cr(VI) was noted here at S1 in FeBC_Si and in BC from the batch
457 experiment (Su et al., 2021), but not in BC from the present column experiment or
458 FeBC from the batch experiment (Su et al., 2021). The differences of LCF results

459 between the column and batch experiments indicate that only the biochars loaded with
460 abundant Fe can completely reduce the adsorbed Cr to trivalent form. These results
461 confirm the key role of Fe in Cr reduction and removal.

462 Cr EXAFS spectra were modeled to reveal the local atomic structures of Cr in
463 the biochars (Fig. 6b-d). The best-fit reference for the samples is $Cr(OH)_3$, and the fits
464 are reasonable with an R-factor ranging from 0.02 to 0.05. The peaks at 1.95 and 3.02
465 Å in R space reflect Cr-O and Cr-Fe bond scattering, respectively. The CNs of Cr-O
466 and Cr-Fe increased from 4.8 to 5.3 and decreased from 2.6 to 2.1 from the bottom to
467 top of FeBC_Si, respectively. Cr EXAFS data reveal that Cr and Fe exist as $Cr_nFe_{(1-n)}(OOH)$ (Eq. 11), corresponding to Cr and Fe in carbon materials calculated by Chen
468
469 et al. (2021) using density functional theory. The higher coordination shell (Cr-Fe) of
470 the S5 sample from FeBC_Ca_BC could not be quantitively resolved.

$$nCr^{3+} + (1-n)Fe^{3+} + H_2O \rightarrow Cr_nFe_{(1-n)}(OOH) + H^+. \quad (11)$$

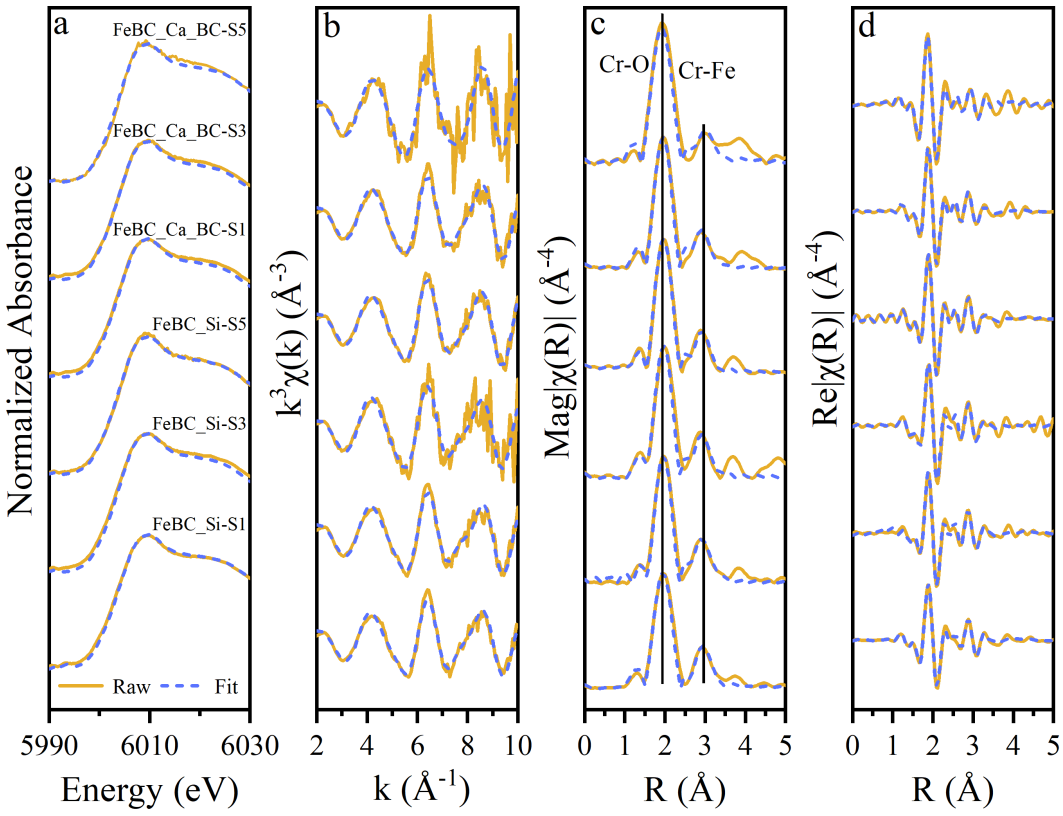

Figure 6. Raw and best fit data for FeBC (ports S1, S3, and S5) of FeBC_Si collected at 102 PVs, and for FeBC (port S1) and BC (ports S3 and S5) of FeBC_Ca_BC collected at 92 PVs for (a) Cr XANES, (b) EXAFS, (c) Fourier-transformed, and (d) Fourier-transformed real-part spectra, respectively.

Table 2. LCF and EXAFS fitting results for biochars (FeBC* at 1 d; FeBC (ports S1, S3, and S5) of FeBC_Si at PV=102; FeBC (port S1) of FeBC_Ca_BC at PV=92; BC* at 1 d; and BC (ports S3 and S5) of FeBC_Ca_BC at PV=92). The ΔE_0 and R-factor values are lower than 4 eV and 0.05, respectively, for all samples.

Sample	LCF		EXAFS			
	Cr(III) (%)	Cr(VI) (%)	Paths	*CN*	*R* (Å)	σ^2 (Å^2)
FeBC*	100	0	Cr-O	4.8(0.6)	1.97(0.01)	0.000
			Cr-Fe	1.7(1.5)	3.02(0.03)	0.005
FeBC_Si-S1	94.5	5.5	Cr-O	4.8(0.6)	1.97(0.01)	0.001
			Cr-Fe	2.6(1.8)	2.99(0.02)	0.008
FeBC_Si-S3	100	0	Cr-O	5.1(0.6)	1.97(0.01)	0.002
			Cr-Fe	2.2(1.3)	2.99(0.02)	0.006
FeBC_Si-S5	100	0	Cr-O	5.3(0.8)	1.98(0.01)	0.001
			Cr-Fe	1.9(1.8)	3.00(0.03)	0.005
FeBC_Ca_BC-S1	100	0	Cr-O	4.8(0.6)	1.97(0.01)	0.000
			Cr-Fe	2.1(1.9)	3.00(0.03)	0.007
BC*	13.1	86.9	Cr-O	4.0(0.5)	1.99(0.01)	0.001
			Cr-Fe	NA	NA	NA
FeBC_Ca_BC-S3	100	0	Cr-O	5.1(0.7)	1.97(0.01)	0.001
			Cr-Fe	1.5(1.4)	2.99(0.03)	0.004
FeBC_Ca_BC-S5	100	0	Cr-O	5.6(2.3)	1.95(0.03)	0.000
			Cr-Fe	NA	NA	NA

Note: *as reported in the batch study conducted by Su et al. (2021).

WT analyses were used to qualitatively resolve Cr backscatter. All of the wavelets of the biochar EXAFS suggest the contributions of the first shell with backscattering maxima are around 5 $Å^{-1}$, corresponding to Cr−O scattering (Fig. 7a-f). The WT analyses reveal similar features corresponding to Cr−Fe scattering in the Fourier transform at k values around 6 $Å^{-1}$, except for sample S5 from FeBC_Ca_BC. A distinctive feature of the higher coordination shell is observed in the EXAFS spectrum of the S5 sample from FeBC_Ca_BC at k values around 6.2 $Å^{-1}$ and R values around 3.4 Å. The differences in energy and distance of backscattering between the S5 sample from FeBC_Ca_BC and the other samples suggests two configurations of inner-sphere complexes exist in the biochars, corresponding to double corner and edge sharing configurations, respectively (Papassiopi et al., 2014). The results indicate a structural transformation of inner-sphere complexes from double corner sharing to edge sharing during Cr(VI) removal.

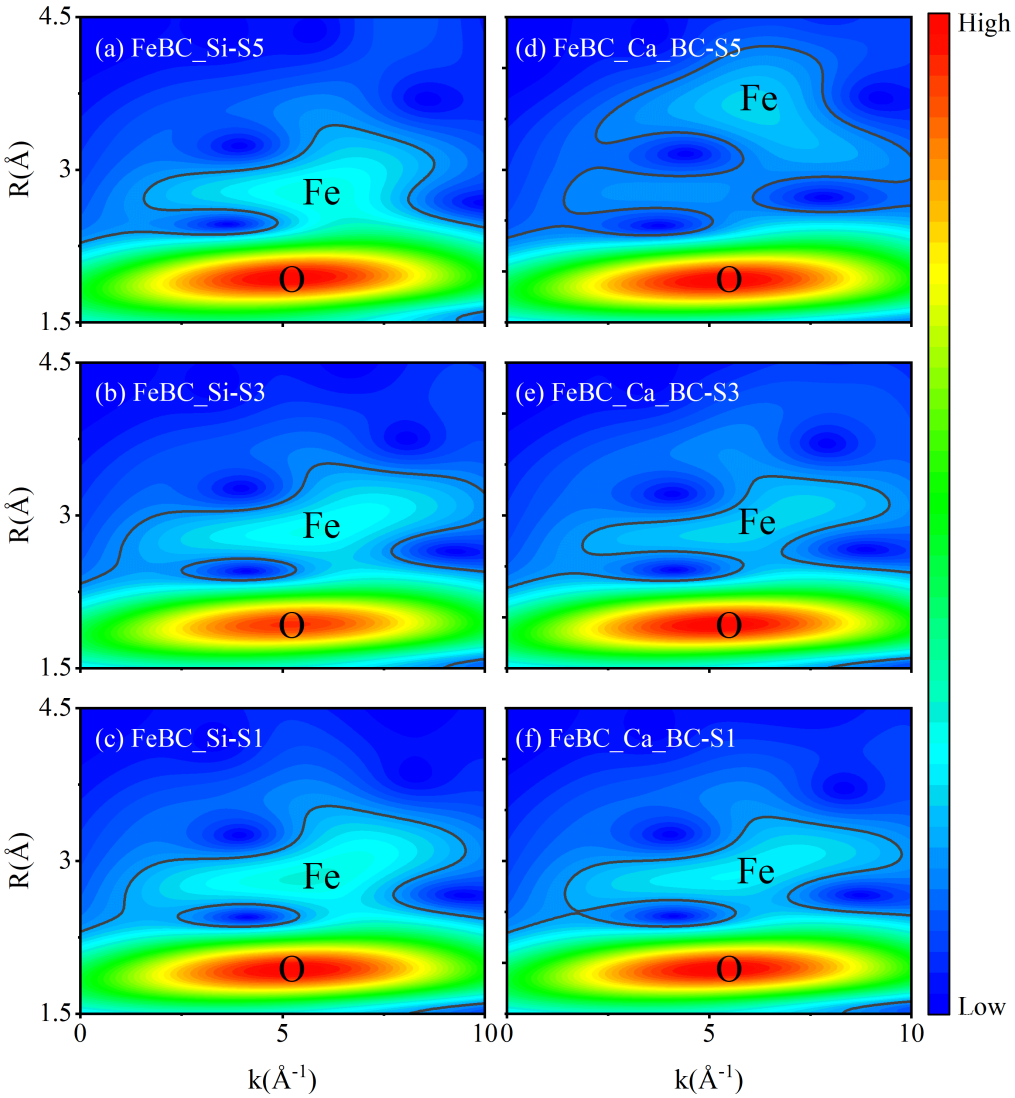

Figure 7. Morlet WT plots of FeBC_Si-S5 displaying the coordination shells (η = 10, σ = 1) for FeBC (ports (a) S5, (b) S3, and (c) S1) of FeBC_Si collected at 102 PVs, and for BC (ports (d) S5 and (e) S3) and FeBC ((f) port S1) of FeBC_Ca_BC collected at 92 PVs.

3.4 Cr(VI) transformation and removal mechanisms

Based on the results of the column experiment, the following Cr(VI) removal mechanisms are proposed. A fraction of Cr(VI) is reduced by aqueous Fe^{2+} (Eq. 12) and then adsorbed on the biochar surface (Eq. 9). The remaining Cr(VI) is initially adsorbed on the biochars (Eq. 8), and reduced by the loaded Fe (Eq. 13) or oxygen-containing functional groups (Eq. 6) on the biochars. In addition to the direct redox reaction, the biochars also act as an electron shuttle to enhance Cr(VI) reduction by

increasing the reactivity of the loaded Fe (Eq. 14) (Xu et al., 2019).

Cr(III) forms a precipitate ($Cr(OH)_3$) or co-precipitate ($Cr_nFe_{(1-n)}(OOH)$) on the biochars or limestone (Eq. 11). Cr and Fe prefer to form inner-sphere complexes and then transform from double corner sharing to edge sharing during the removal. Gradually, the surface Cr penetrates into the interior of the biochars and becomes a more stable species (Eq. 10). Mechanisms for enhanced Cr(VI) removal in FeBC_Ca_BC are also proposed here. The addition of BC and limestone can balance the pH of the columns and immobilize the leached Fe (Eqs. 7&15). The elevated pH reduces the acidic corrosion of FeBC, and the final pH also matches the optimum pH for co-precipitation of Cr and Fe (Gheju and Balcu, 2011). Further, BC is able to remove Cr(VI) in a similar pathway as for FeBC after immobilizing the aqueous Fe (Eq. 3).

$$Fe^{2+} + Cr_2O_7{}^{2-} + H^+ \rightarrow Fe^{3+} + Cr^{3+} + H_2O, \quad (12)$$

$$\equiv R - Fe + Cr_2O_7{}^{2-} + H^+ \rightarrow \equiv R + Fe^{3+} + Cr^{3+} + H_2O, \quad (13)$$

$$\equiv R - Fe(\text{minerals}) + Cr_2O_7{}^{2-} + H^+ \xrightarrow{biochar} \equiv R + Fe^{3+} + Cr^{3+} + H_2O, \quad (14)$$

$$CaCO_3 + H^+ \rightarrow Ca^{2+} + CO_2 + H_2O. \quad (15)$$

4. Conclusion

This study developed a low-cost bilayer PRB filled with two synergistic biochars to remediate Cr(VI)-contaminated groundwater. Although FeBC has a high Cr(VI) removal capacity as a reactive material in a PRB under saturated conditions, the leached Fe and acidic effluent are likely to cause risks to the environment. The excess corrosion of FeBC leads to the leaching of Fe and is sensitive to pH and Cr(VI)

concentration rather than the flow rate. The different driving forces of solute transport (convection for Fe^{2+} and diffusion for H^{+}) caused by the concentration gradient were considered to develop the bilayer PRBs and exploit the advantages of both FeBC and BC. The results suggest the environmental risk of Fe leached from FeBC can be successfully mitigated by the addition of BC and limestone. The removal capacity of FeBC in the bilayer column featuring FeBC, limestone, and BC was the highest of the configurations tested. Based on evidence gathered from synchrotron-related techniques, the enhancement provided by the addition of BC and limestone to the FeBC column can be summarized as follows: (1) Fe released from the FeBC in the first layer is immobilized and reutilized; and (2) the pH is balanced to reduce the acidic corrosion of FeBC and facilitate the co-precipitation of Cr and Fe.

Overall, this study evaluated and improved the long-term performance of FeBC-based PRBs for alkaline groundwater environments and immobilized the leached Fe. The novel bilayer PRBs had better Cr(VI) removal efficiencies and less leached Fe than reported in previous studies. Furthermore, this study is the first to propose a structural transformation of inner-sphere complexes from double corner sharing to edge sharing during Cr(VI) removal by FeBC. The combined utilization of multiple materials to develop the bilayer PRB in this study is a potential remediation strategy for the removal of Cr(VI) from groundwater. More studies are required to investigate the role of anaerobic autotrophic bacteria during Cr(VI) removal by FeBC-based bilayer PRBs, due to the long running time and high concentration of inorganic carbon. The application of a geochemical model to quantify the contributions of

546 adsorption and reduction during the removal could further clarify the removal
547 mechanisms and guide the application of FeBC-based PRBs.

548 **Acknowledgements**

549 This research was supported by the National Key Research and Development
550 Program of China [grant number 2018YFC1801700] and National Natural Science
551 Foundation of China [grant number 41877478]. Synchrotron analyses were performed
552 at Beamlines 9-BM, 20-BM, and 20-ID of the Advanced Photon Source, Argonne
553 National Laboratory.

554

References

Ahmed, M.B., Zhou, J.L., Ngo, H.H., Guo, W., Johir, M.A.H., Sornalingam, K., Belhaj, D. and Kallel, M., 2017. Nano-Fe^0 immobilized onto functionalized biochar gaining excellent stability during sorption and reduction of chloramphenicol via transforming to reusable magnetic composite. Chem. Eng. J. 322, 571-581. doi:10.1016/j.cej.2017.04.063.

An, Q., Li, X.Q., Nan, H.Y., Yu, Y. and Jiang, J.N., 2018. The potential adsorption mechanism of the biochars with different modification processes to Cr(VI). Environ. Sci. Pollut. Res. 25(31), 31346-31357. doi:10.1007/s11356-018-3107-7.

Aziz, H.A., Adlan, M.N. and Ariffin, K.S., 2008. Heavy metals (Cd, Pb, Zn, Ni, Cu and Cr(III)) removal from water in Malaysia: post treatment by high quality limestone. Bioresour. Technol. 99(6), 1578-1583. doi:10.1016/j.biortech.2007.04.007.

Blowes, D., 2002. Environmental chemistry. Tracking hexavalent Cr in groundwater. Science 295(5562), 2024-2025. doi:10.1126/science.1070031.

Blowes, D.W., Ptacek, C.J. and Jambor, J.L., 1997. In-situ remediation of Cr(VI)-contaminated groundwater using permeable reactive walls: laboratory studies. Environ. Sci. Technol. 31(12), 3348-3357. doi:10.1021/es960844b.

Chaparro, A.M., Maffiotte, C., Gutiérrez, M.T. and Herrero, J., 2000. Morphological and compositional study of CBD-ZnSe thin films by microscopy techniques and angle resolved XPS. Thin Solid Films 358(1), 22-29. doi:10.1016/S0040-6090(99)00704-X.

Chen, J., Wu, H., Xu, L., Li, M., Du, K. and Sheng, G., 2021. New insights into colloidal GO, Cr(VI) and Fe(II) interaction by a combined batch, spectroscopic and DFT calculation investigation. J. Mol. Liq. 337, 116365. doi:10.1016/j.molliq.2021.116365.

Choudhary, B., Paul, D., Singh, A. and Gupta, T., 2017. Removal of hexavalent chromium upon interaction with biochar under acidic conditions: mechanistic insights and application. Environ. Sci. Pollut. Res. 24(20), 16786-16797. doi:10.1007/s11356-017-9322-9.

Choudhury, A. and Lansing, S., 2020. Biochar addition with Fe impregnation to reduce H_2S production from anaerobic digestion. Bioresour. Technol. 306, 123121. doi:10.1016/j.biortech.2020.123121.

Diao, Z.-H., Xu, X.-R., Jiang, D., Kong, L.-J., Sun, Y.-X., Hu, Y.-X., Hao, Q.-W. and Chen, H., 2016. Bentonite-supported nanoscale zero-valent iron/persulfate system for the simultaneous removal of Cr(VI) and phenol from aqueous solutions. Chem. Eng. J. 302, 213-222. doi:10.1016/j.cej.2016.05.062.

Feng, Y., Liu, P., Wang, Y.X., Finfrock, Y.Z., Xie, X.J., Su, C.L., Liu, N., Yang, Y.Y. and Xu, Y., 2020. Distribution and speciation of iron in Fe-modified biochars and its application in removal of As(V), As(III), Cr(VI), and Hg(II): an X-ray absorption study. J. Hazard. Mater. 384, 121342. doi:10.1016/j.jhazmat.2019.121342.

598 Funke, H., Scheinost, A.C. and Chukalina, M., 2005. Wavelet analysis of extended x-
599 ray absorption fine structure data. Phys. Rev. B 71(9), 094110.
600 doi:10.1103/PhysRevB.71.094110.
601 Gheju, M. and Balcu, I., 2011. Removal of chromium from Cr(VI) polluted
602 wastewaters by reduction with scrap iron and subsequent precipitation of
603 resulted cations. J. Hazard. Mater. 196, 131-138.
604 doi:10.1016/j.jhazmat.2011.09.002.
605 Guo, X., Yang, Z., Dong, H., Guan, X., Ren, Q., Lv, X. and Jin, X., 2016. Simple
606 combination of oxidants with zero-valent-iron (ZVI) achieved very rapid and
607 highly efficient removal of heavy metals from water. Water Res. 88, 671-680.
608 doi:10.1016/j.watres.2015.10.045.
609 He, R., Yuan, X., Huang, Z., Wang, H., Jiang, L., Huang, J., Tan, M. and Li, H., 2019.
610 Activated biochar with iron-loading and its application in removing Cr(VI)
611 from aqueous solution. Colloid Surf. A-Physicochem. Eng. Asp. 579, 123642.
612 doi:10.1016/j.colsurfa.2019.123642.
613 Huang, Y., Zeng, Q., Hu, L., Xiong, D., Zhong, H. and He, Z., 2021. Column study of
614 enhanced Cr(VI) removal and removal mechanisms by *Sporosarcina*
615 *saromensis* W5 assisted bio-permeable reactive barrier. J. Hazard. Mater. 405,
616 124115. doi:10.1016/j.jhazmat.2020.124115.
617 Jamieson-Hanes, J.H., Amos, R.T., Blowes, D.W. and Ptacek, C.J., 2015. Dual
618 mechanism conceptual model for Cr isotope fractionation during reduction by
619 zerovalent iron under saturated flow conditions. Environ. Sci. Technol. 49(9),
620 5467-5475. doi:10.1021/es506223a.
621 Kantar, C., Ari, C. and Keskin, S., 2015. Comparison of different chelating agents to
622 enhance reductive Cr(VI) removal by pyrite treatment procedure. Water Res.
623 76, 66-75. doi:10.1016/j.watres.2015.02.058.
624 Li, P., Wang, Q., He, X., Yu, R., He, C., Shen, D. and Jiao, Y., 2022a. Investigation on
625 the effect of different additives on anaerobic co-digestion of corn straw and
626 sewage sludge: comparison of biochar, Fe_3O_4, and magnetic biochar.
627 Bioresour. Technol. 345, 126532. doi:10.1016/j.biortech.2021.126532.
628 Li, S., You, T., Guo, Y., Yao, S., Zang, S., Xiao, M., Zhang, Z. and Shen, Y., 2019.
629 High dispersions of nano zero valent iron supported on biochar by one-step
630 carbothermal synthesis and its application in chromate removal. Rsc Adv.
631 9(22), 12428-12435. doi:10.1039/C9RA00304E.
632 Li, Y., Shao, M., Huang, M., Sang, W., Zheng, S., Jiang, N. and Gao, Y., 2022b.
633 Enhanced remediation of heavy metals contaminated soils with EK-PRB using
634 β-CD/hydrothermal biochar by waste cotton as reactive barrier. Chemosphere
635 286, 131470. doi:10.1016/j.chemosphere.2021.131470.
636 Liu, P., Ptacek, C.J., Blowes, David W. and Finfrock, Y.Z., 2017. A beam path-based
637 method for attenuation correction of confocal micro-X-ray fluorescence
638 imaging data. J. Anal. At. Spectrom. 32(8), 1582-1589.
639 doi:10.1039/C7JA00148G.
640 Liu, P., Ptacek, C.J., Blowes, D.W. and Finfrock, Y.Z., 2019a. Mercury distribution
641 and speciation in biochar particles reacted with contaminated sediment up to

1030 days: a synchrotron-based study. Sci. Total Environ. 662, 915-922. doi:10.1016/j.scitotenv.2019.01.148.
Liu, P., Ptacek, C.J., Blowes, D.W., Finfrock, Y.Z., Steinepreis, M. and Budimir, F., 2019b. A method for redox mapping by confocal micro-X-ray fluorescence imaging: using chromium species in a biochar particle as an example. Anal. Chem. 91(8), 5142-5149. doi:10.1021/acs.analchem.8b05718.
Liu, W., Feng, Y., Zhong, H., Ptacek, C., Blowes, D., Liu, Y., Finfrock, Y.Z., Liu, P. and Wang, S., 2020. Aqua regia digestion cannot completely extract Hg from biochar: a synchrotron-based study. Environ. Pollut. 265, 115002. doi:10.1016/j.envpol.2020.115002.
Lu, Q., Jeen, S.-W., Gui, L. and Gillham, R.W., 2017. Nitrate reduction and its effects on trichloroethylene degradation by granular iron. Water Res. 112, 48-57. doi:10.1016/j.watres.2017.01.031.
Mineno, T. and Okazaki, M., 2004. Adsorption of Cr(VI) ion on synthetic hydrated oxides of iron. Soil Sci. Plant Nutr. 50(7), 1043-1046. doi:10.1080/00380768.2004.10408572.
Noubactep, C., 2022. Should the term ‘metallic iron’ appear in the title of a research paper? Chemosphere 287, 132314. doi:10.1016/j.chemosphere.2021.132314.
Papassiopi, N., Pinakidou, F., Katsikini, M., Antipas, G.S.E., Christou, C., Xenidis, A. and Paloura, E.C., 2014. A XAFS study of plain and composite iron(III) and chromium(III) hydroxides. Chemosphere 111, 169-176. doi:10.1016/j.chemosphere.2014.03.059.
Park, D., Yun, Y.-S. and Park, J.M., 2008. XAS and XPS studies on chromium-binding groups of biomaterial during Cr(VI) biosorption. J. Colloid Interface Sci. 317(1), 54-61. doi:10.1016/j.jcis.2007.09.049.
Peña, J., Kwon, K.D., Refson, K., Bargar, J.R. and Sposito, G., 2010. Mechanisms of nickel sorption by a bacteriogenic birnessite. Geochim. Cosmochim. Acta 74(11), 3076-3089. doi:10.1016/j.gca.2010.02.035.
Ravel, B. and Newville, M., 2005. ATHENA, ARTEMIS, HEPHAESTUS: data analysis for X-ray absorption spectroscopy using IFEFFIT. J. Synchrotron Radiat. 12(4), 537-541. doi:10.1107/S0909049505012719.
Richard, J.-H. and Biester, H., 2016. Mercury removal from contaminated groundwater: performance and limitations of amalgamation through brass shavings. Water Res. 99, 272-280. doi:10.1016/j.watres.2016.05.007.
Sleiman, N., Deluchat, V., Wazne, M., Mallet, M., Courtin-Nomade, A., Kazpard, V. and Baudu, M., 2016. Phosphate removal from aqueous solution using ZVI/sand bed reactor: behavior and mechanism. Water Res. 99, 56-65. doi:10.1016/j.watres.2016.04.054.
Su, C., Wang, S., Zhou, Z., Wang, H., Xie, X., Yang, Y., Feng, Y., Liu, W. and Liu, P., 2021. Chemical processes of Cr(VI) removal by Fe-modified biochar under aerobic and anaerobic conditions and mechanism characterization under aerobic conditions using synchrotron-related techniques. Sci. Total Environ. 768, 144604. doi:10.1016/j.scitotenv.2020.144604.
Trakal, L., Bingöl, D., Pohořelý, M., Hruška, M. and Komárek, M., 2014.

686 Geochemical and spectroscopic investigations of Cd and Pb sorption
687 mechanisms on contrasting biochars: engineering implications. Bioresour.
688 Technol. 171, 442-451. doi:10.1016/j.biortech.2014.08.108.
689 Tu, C., Wei, J., Guan, F., Liu, Y., Sun, Y. and Luo, Y., 2020. Biochar and bacteria
690 inoculated biochar enhanced Cd and Cu immobilization and enzymatic
691 activity in a polluted soil. Environ. Int. 137, 105576.
692 doi:10.1016/j.envint.2020.105576.
693 Wiegand, B.A., 2009. Tracing effects of decalcification on solute sources in a shallow
694 groundwater aquifer, NW Germany. J. Hydrol. 378(1), 62-71.
695 doi:10.1016/j.jhydrol.2009.09.013.
696 Wilkin, R.T., Su, C., Ford, R.G. and Paul, C.J., 2005. Chromium-removal processes
697 during groundwater remediation by a zerovalent iron permeable reactive
698 barrier. Environ. Sci. Technol. 39(12), 4599-4605. doi:10.1021/es050157x.
699 Xu, X., Huang, H., Zhang, Y., Xu, Z. and Cao, X., 2019. Biochar as both electron
700 donor and electron shuttle for the reduction transformation of Cr(VI) during its
701 sorption. Environ. Pollut. 244, 423-430. doi:10.1016/j.envpol.2018.10.068.
702 Ye, Z., Zhou, J., Liao, P., Finfrock, Y.Z., Liu, Y., Shu, C. and Liu, P., 2022. Metal (Fe,
703 Cu, and As) transformation and association within secondary minerals in
704 neutralized acid mine drainage characterized using X-ray absorption
705 spectroscopy. Appl. Geochem. 139, 105242.
706 doi:10.1016/j.apgeochem.2022.105242.
707 Zhang, W., Gao, M., Miao, F., Wu, X., Wang, S. and Wang, X., 2021. A permeable
708 electrochemical reactive barrier for underground water remediation using
709 TiO_2/graphite composites as heterogeneous electrocatalysts without releasing
710 of chemical substances. J. Hazard. Mater. 418, 126318.
711 doi:10.1016/j.jhazmat.2021.126318.
712 Zhao, N., Zhao, C., Tsang, D.C.W., Liu, K., Zhu, L., Zhang, W., Zhang, J., Tang, Y.
713 and Qiu, R., 2021. Microscopic mechanism about the selective adsorption of
714 Cr(VI) from salt solution on O-rich and N-rich biochars. J. Hazard. Mater. 404,
715 124162. doi:10.1016/j.jhazmat.2020.124162.
716 Zhong, J., Yin, W., Li, Y., Li, P., Wu, J., Jiang, G., Gu, J. and Liang, H., 2017. Column
717 study of enhanced Cr(VI) removal and longevity by coupled abiotic and biotic
718 processes using Fe^0 and mixed anaerobic culture. Water Res. 122, 536-544.
719 doi:10.1016/j.watres.2017.05.043.
720